Title

DISCHARGE OXIDE STORAGE CAPACITY AND VOLTAGE LOSS IN LI-AIR BATTERY

Permalink

https://escholarship.org/uc/item/3wz2c7g7

Authors

Wang, Yun
Wang, Zhe
Yuan, Hao
et al.

Publication Date

2015-10-01

DOI

10.1016/j.electacta.2015.08.121

Peer reviewed

DISCHARGE OXIDE STORAGE CAPACITY AND VOLTAGE LOSS IN LI-AIR BATTERY

Yun Wang[a,*], Zhe Wang[b], Hao Yuan[a], Tianqi Li[b]

[a] Renewable Energy Resources Lab (RERL), Department of Mechanical and Aerospace Engineering, The University of California, Irvine, CA 92697-3975, United States
[b] State Key Laboratory of Power Systems, Department of Thermal Engineering, Tsinghua University, Beijing 100084, PR China

ABSTRACT

Air cathodes, where oxygen reacts with Li ions and electrons with discharge oxide stored in their pore structure, are often considered as the most challenging component in nonaqueous Lithium-air batteries. In non-aqueous electrolytes, discharge oxides are usually insoluble and hence precipitate at local reaction site, raising the oxygen transport resistance in the pore network. Due to their low electric conductivity, their presence causes electrode passivation. This study aims to investigate the air cathode's performance through analytically obtaining oxygen profiles, modeling electrode passivation, evaluating the transport polarization raised by discharge oxide precipitate, and developing analytical formulas for insoluble Li oxides storage capacity. The variations of cathode quantities, including oxygen content and temperature, are evaluated and related to a single dimensionless parameter — the Damköhler Number (Da). An approximate model is developed to predict discharge voltage loss, along with validation against two sets of experimental data. Air cathode properties, including tortuosity, surface coverage factor and the Da number, and their effects on the cathode's capacity of storing Li oxides are formulated and discussed.

1. Introduction

Li-air batteries hold a great promise for high specific energy storage. Bruce et al. [1] reported a theoretical value of 3,505 Wh kg^{-1} using non-aqueous electrolytes, which is much closer to those of direct methanol fuel cells (DMFC) (5,524 Wh kg^{-1}) and gasoline engine (11,860 Wh kg^{-1}) than conventional Li-ion batteries. Fig. 1 shows the schematic of a Li-air battery and its discharge operation. During discharge, lithium is oxidized in the anode to produce lithium ions and electrons: electrons are conducted via an external circuit to produce electric work, while lithium ions are transported across electrolyte to react with oxygen and electrons in the cathode. During charging, lithium metal is plated out in the anode, and O$_2$ is released in the cathode.

Air cathodes are often considered as the most challenging component in nonaqueous Lithium-air batteries. In cathodes, oxygen is reduced to produce Li composites during discharge, e.g. lithium oxides:

$$Li^+e^- + O_2 + ^* \rightarrow LiO_2^*$$

$$Li^+e^- + LiO_2^* \rightarrow Li_2O_2^* \qquad (1)$$
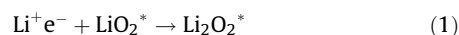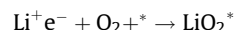
where "*" denotes a surface site on the reaction surface or oxides in which the growth proceeds. Air cathode contributes a major voltage loss because of the sluggish reaction kinetics and oxygen transport. In addition, oxide products are usually insoluble in non-aqueous electrolytes, causing pore-network clogging. Li oxide composites are low in electric conductivity, thus their presence on the reaction surface resists electron's access to reaction sites, causing electrode passivation. As discharging proceeds, oxide precipitate accumulates in the pore networks and on the reaction surface, increasing both oxygen and electron transport resistances, and consequently voltage loss.

The first non-aqueous rechargeable Li-air batteries were reported by Abraham and Jiang in 1996 [2]. Since then, the technology has received a fast growing interest of research to explore electrochemical reaction mechanisms, electrode structures, and electrolyte and catalyst materials [3–9]. Mirzaeian and Hall studied the impacts of porosity, pore structure, morphology of carbon and surface area of carbon in air cathodes on the battery's specific capacity [10]. Pore structure was adjusted by controlling the molar ratio of resorcinol to catalyst and the pyrolysis and activation temperatures. They found that the battery performance

* Corresponding author. Tel.:+ 949-824-6004; fax: +949-824-8585.
E-mail address: yunw@uci.edu (Y. Wang).

Nomenclature

a   factor of effective catalyst area per unit volume when oxide precipitate is present
a_o factor of catalyst surface area factor per unit volume
C   molar concentration of species k, mol/m^3
D   species diffusivity, m^2/s
Da   the Damköhler Number
F   Faraday's constant, 96,487C/mol
I   current density, A/cm^2
i   superficial current density, A/cm^2
j   transfer current density, A/cm^3
M   molecular weight, kg/mol
R   universal gas constant, 8.134 J/mol K; Ohmic resistance, mΩ cm^2
s   volume fraction of Li oxide in pores
s_{max} maximum volume fraction of Li oxide in pores
t   time, s
T   temperature, K

Greek
β   transfer coefficient
ρ density, kg/m^3
ϕ phase potential, V
κ ionic conductivity, S/m
ε porosity or volume fraction
η surface overpotential, V
τ_a coverage coefficient by oxide deposit
τ_d tortuosity of air cathode
δ thickness, m

Superscripts and Subscripts
a   surface coverage
c   cathode
d   diffusion
e   electrolyte
eff   effective value
o   reference value; initial value
max   maximum

changes with the morphology of carbon, the pore volume, pore size, and surface area of carbon. Yang et al. used mesocellular carbon foam as the cathode [11]. They fabricated carbon samples containing bimodal mesopores with a narrow pore size distribution through nanocasting technique; and showed the samples yielded about 40% capacity increase compared with commercial carbon black. Mitchell et al. used hollow carbon fibers of 30 nm diameters grown on ceramic porous substrate in air cathodes [12], and achieved a high specific capacity under low carbon loading. They also indicated Li oxides grew as nodules on the fibers and developed into toroids during discharge. Griffith et al. [13] observed Li oxides form typical 'toroidal' particles under low discharge rates, and take needle-like shapes under the high rates, instead of the nano-sheets or compact films. They indicated Li_2O_2 grows by a locally mass-transfer-limited nucleation and growth mechanism. Xiao et al. [14] investigated the effects of carbon microstructure and loading on battery performance. They found that the cathode capacity increased with the carbon source's mesopore volume, and that the pore size's uniformity played an important role in battery performance. Zhang et al. [15] employed galvanostatic discharge, polarization, and AC-impedance techniques to study Li-air battery, showing that the discharge performance is determined mainly by air cathode, instead of Li anode. Viswanathan et al. [16] employed a reversible redox couple to investigate the deposit film resistance and adopted a metal-insulator-metal charge transport model to predict the electrical conductivity of a Li_2O_2 film. They showed "sudden death" in the charge transport when the film thickness is approximately 5 nm to 10 nm.<

In modeling and analysis, Franc and Xue [17] discussed the carbon-based electrode models from the atomistic to continuum approaches, and briefly introduced a new theory to study the impact of the electrode's carbon structure on battery's cyclability. Andrei et al. [18] discussed several approaches to improve the battery's energy density. They concluded that it is more efficient to use non-uniform catalyst, which enhances the reaction at the separator–cathode interface, than to use uniform catalyst. They also discussed energy density improvement through solvents with high oxygen solubility/diffusivity and partly wetted electrodes. Albertus et al. proposed a physics-based model accounting for oxide precipitates [19]. They developed a film growth model over a spherical carbon particle; and proposed an electric resistance formula for the oxide film. Following the Li-ion battery approach, a
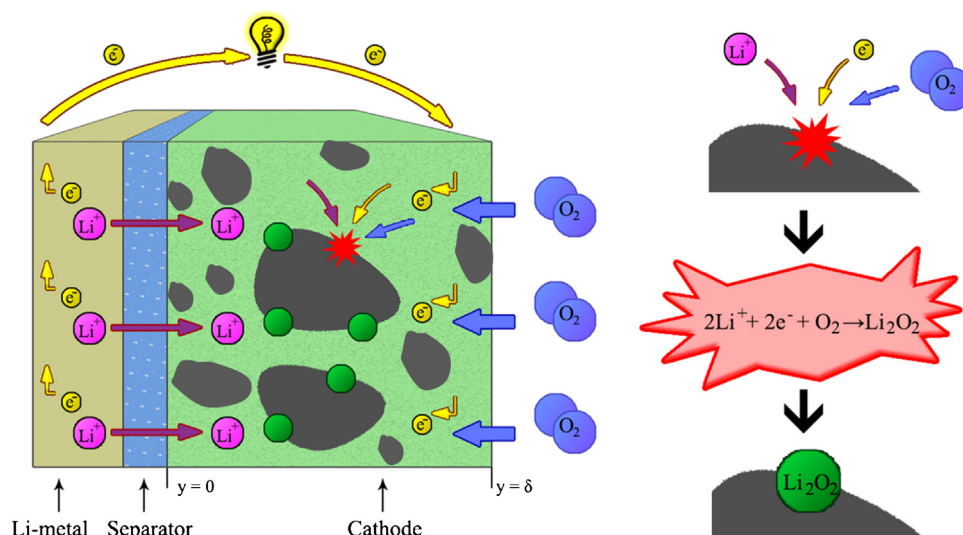

Fig. 1. Schematic of a Li-air battery and its discharge operation with Li_2O_2 as an example of discharge product. y starts at the interface between the separator and cathode electrode; and δ denotes the cathode electrode thickness.

1-D Li-air battery model was developed and validated with experimental data. Sandhu et al. [20] developed a diffusion-limited model assuming a cylindrical pore morphology, and presented the transient concentration profiles of the dissolved oxygen in the electrolyte using numerical iterative methods. Battery capacities were predicted and compared with literature experimental results. Nanda et al. [21] reported a three-dimensional spatial distribution of lithium products using neutron tomographic imaging. They observed a higher concentration of lithium oxides near the edge of electrode; and a relatively uniform distribution in the center area. Similar phenomena were also reported by Wang and Cho [22], who developed a multi-dimensional model based on the conservation law of Li^+, oxygen, and charges, in conjunction of the electrochemical reaction kinetics. They showed non-uniform distribution in the reaction rate is more remarkable under higher current and explained the sluggish oxygen transport is the primary cause. They also analyzed the oxygen content variation in the supply channel, indicating it is determined by a dimensionless number and thin channels is desirable to achieve high energy density without sacrificing oxygen supply. Wang [23] pointed out that lithium oxide precipitation is similar to water freezing in PEM fuel cells under sub-freezing condition, and explained the similarity between ice formation within PEM fuel cells [24,25] and oxide precipitate in Li-air batteries. A coverage model was developed to account for oxide precipitate's effects, and validated against the experimental data for planar electrodes. Wang and Cho [26] further extended the fuel cell knowledge [27] to Li-air battery by developing the formula of the voltage losses due to electrode passivation and oxygen transport resistance, respectively, raised by oxide precipitate. Their analysis indicated that the electrode

passivation contributes the major voltage loss at the beginning of discharge, while the oxygen resistance can be significant near the "sudden death".

Though a great deal of effort was made in Li-air battery development, most were focused on the aspects of material development and electrochemistry exploration. Theoretical analysis is largely lacked at current stage, particularly those that can be directly applied for battery design and optimization, specially those analytical formulas that directly relate battery performance or Li oxide storage capacity to material properties and operating condition. In this paper, we investigate the air cathode performance through defining a single dimensionless parameter to evaluate the spatial variation of important cathode quantities, analytically obtaining oxygen profiles, modeling battery performance by accounting for both electrode passivation and oxygen transport polarization, and formulating the capacity of Li oxides storage. Oxygen profiles are obtained under various conditions, along with the oxygen transport polarization. For the first time, formulas are derived to relate several important parameters, including tortuosity, surface coverage, and Da, to the capacity of storing Li oxide deposit in air cathodes.

2. The Damköhler Number

During operation, the energy conversion inefficiency gives rise to thermal energy release and consequent temperature gradient. A large temperature variation will have profound effects on Li-air battery operation as temperature determines the capability of overcoming the activation barrier of a reaction. The principle mechanisms for waste heat generation include the reversible and

Table 1
Ionic conductivity for various electrolytes [26]

Electrolyte	Ionic conductivity	Remarks	Reference
PVA (Poly Vinyl Alcohol)	$10^{-8} \sim 10^{-4}$ S/cm	PVA complexed with lithium triflate system	[33]
PC / γ-BL (propylenecarbonate / γ-butyrolactone)	1.7×10^{-3} S/cm	60P(ECH-EO):15PC:10γ-BL:15LiClO$_4$ @ 363K	[34]
DMF / γ-BL (dimethylformamide / γ-butyrolactone)	2.8×10^{-3} S/cm	60P(ECH-EO):15DMF:10γ-BL:15LiClO$_4$ @ 363K	
PVA(15)–PMMA(10)–LiBF4(8)– EC(67)	9.0377×10^{-3} S/cm	@373K	[35]
PVA(15)–PMMA(10)–LiBF4(8)– PC(67)	2.4855×10^{-3} S/cm		
PVA(15)–PMMA(10)–LiBF4(8)– DEC(67)	0.2022×10^{-3} S/cm		
PVA(15)–PMMA(10)–LiBF4(8)– GBL(67)	1.1523×10^{-3} S/cm		
PVdF- HFP	2×10^{-3} S/cm		[36]
PVC / PMMA	1.4×10^{-3} S/cm	@ room temperature	[37]
PAN(21)–PEO(2)– LiCF$_3$SO$_3$ (8)–PC(27.7)–EC(41.3)	1.713×10^{-3} S/cm	@373K	[38]
PAN(21)–PEO(5)– LiCF$_3$SO$_3$ (8)–PC(24.7)–EC(41.3)	8.492×10^{-3} S/cm		
PAN(21)–PEO(10)– LiCF$_3$SO$_3$ (8)–PC(27.7)–EC(33.3)	80.950×10^{-3} S/cm		
PAN(21)–PEO(15)– LiCF$_3$SO$_3$ (8)–PC(24.7)–EC(31.3)	23.880×10^{-3} S/cm		
EC(38) –PC(33) –PAN(21) –LiClO$_4$(8)	3.5×10^{-3} S/cm	@323K	[39]
EC(42) –PC(36) –PAN(15) –LiCF$_3$SO$_3$(7)	2.2×10^{-3} S/cm		
EC(62) –PC(13) –PAN(16) –PEGDA(1) –LiClO$_4$(8)	3.0×10^{-3} S/cm		
EC(68) –PC(15) –PEGDA(3) –LiClO$_4$(14)	8.0×10^{-3} S/cm		
EC(35) –PC(31) –PVP(24) – LiCF$_3$SO$_3$ (10)	1.0×10^{-3} S/cm		
EC–LiClO$_4$	$10^{-8} \sim 10^{-7}$ S/cm	[EC]/[LiClO$_4$] = 0.5 @ 298K	[40]
	10^{-6} S/cm	[EC]/[LiClO$_4$] = 1.0 @ 298K	
	$10^{-5} \sim 10^{-4}$ S/cm	[EC]/[LiClO$_4$] = 2.0 @ 298K	
PEO(22.7) –PAN(17.4) –PrC(7.3) –EC(8.5) –LiClO$_4$(4.3)	0.37×10^{-3} S/cm	HSPE @ 303K	[41]
PEO(22.7) –PrC(13.3) –LiClO$_4$(1.2)	0.84×10^{-3} S/cm	PEO + PrC @ 303K	
PAN(23.2) –PrC(24.5) –EC(28.4) –LiClO$_4$(3.0)	1.34×10^{-3} S/cm	PAN + PrC + EC @ 303K	
PC-DME	10^{-3} S/cm	(1:1 by wt.) plasticized P(LiOEG$_n$B) n=3, 5, 9	[42]
	12×10^{-3} S/cm	(1:1 by vol.) 1 M LiClO$_4$ @ 293K	[43]
	14×0^{-3} S/cm	(1:1 by vol.) 1 M LiPF$_6$ @ 293K	
EC-DMC	8×10^{-3} S/cm	(1:1 by vol.) 1 M LiClO$_4$ @ 293K	
	10×10^{-3} S/cm	(1:1 by vol.) 1 M LiPF$_6$ @ 293K	
	11.7×10^{-3} S/cm	(1:1 by mol) 1 M LiPF$_6$@ 303K	[44]
	$< 10^{-3}$ S/cm	(1:2 by wt.) plasticized P(LiOEG$_n$B) n=3	[45]
DME	5.52×10^{-3} S/cm	1 mol LiF + 1 mol (C$_6$F$_5$)$_3$B in DME	[46]
	7.43×10^{-3} S/cm	1 mol CF$_3$CO$_2$Li + 1 mol (C$_6$F$_5$)$_3$B in DME	
	$5.52 \times 1 \ 10^{-3}$ S/cm	1 mol C$_2$F$_5$CO$_2$Li + 1 mol (C$_6$F$_5$)$_3$B in DME	

irreversible heats of the electrochemical reactions, and ohmic heat. The reversible and irreversible sources are released at the reaction interface during energy conversion, whereas the ohmic heating arises from the resistance to the electric current flow and ion movement. The upper bound of temperature variation can be evaluated by [27]:

$$\Delta T = \frac{I(E' - V_{cell})\delta}{2k^{eff}} \tag{2}$$

where E' is defined as $-\frac{\Delta \overline{h}}{2F}$ and represents the EMF (electromotive force) that all the energy from the Li-oxygen reaction, the 'calorific value', heating value, or enthalpy of formation, were transformed into electrical energy. k^{eff} of 1.0 W/m K, 2.5 V, and 1 mA/cm^2 will yield ΔT approximately 0.01 °C. Under 0.1 A/cm^2 or higher, ΔT will be approximately 1 °C or higher.

In discharging, Li$^+$, oxygen, and electrons are consumed in the cathode. The primary driving forces for the reactant supply are the gradients of their concentrations (for Li$^+$ and oxygen) and electric phase potentials (for ions and electrons). Assuming diffusion and migration dominate Li$^+$ transport, and diffusion is the major driving force for oxygen transport, their spatial variations can be evaluated by:

$$\frac{\Delta C_e}{C_{e,0}} = \frac{(1 - t_+^0)I}{2F} \frac{\delta}{C_{e,0}D_{Ce}^{eff}} \text{ and } \frac{\Delta C_{O2}}{C_{O2,\delta}} = \frac{I}{8F} \frac{\delta}{C_{O2,\delta}D_{O2}^{eff}} \tag{3}$$

where $C_{e,0}$ and $C_{O2,\delta}$ are the concentrations of Li$^+$ and oxygen at y=0 and y=δ (see Fig. 1), respectively, and the transference number of Li$^+$, t_+^0, represents the fraction of the current carried by species Li$^+$. The values of t_+^0 for a few electrolytes are summarized in Ref. [22]. The effective coefficients of material properties can be evaluated through the Bruggeman correlation:

$$D_{Ce}^{eff} = \varepsilon^{\tau_d}D_{Ce}^0 \text{ and } D_{O2}^{eff} = \varepsilon^{\tau_d}D_{O2}^0 \tag{4}$$

The electrolyte phase potential variation can be evaluated by Ohm's law:

$$\Delta \Phi^{(e)} = \frac{I\delta}{2\kappa^{eff}} \tag{5}$$

The variation is approximately 0.001 V under κ^{eff} of 1 S/m, 1 mA/cm^2 and δ of 0.1 mm. It can be considerable using Low-conductivity electrolyte. Table 1 lists the ionic conductivity for a number of typical electrolytes.

A Damköhler (Da) number can be defined based on oxygen diffusivity as below [27]:

$$Da = \frac{I}{8F} \frac{\delta}{C_{O2,\delta}D_{O2}^{eff}} = \frac{\text{Reaction rate}}{\text{Mass transport rate}} \tag{6}$$
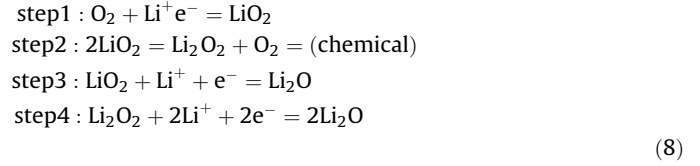
With the definition of the Da number, one can rewrite the above formula of variations as below:

$$\frac{\Delta C_{O2}}{C_{O2,\delta}} = \frac{\Delta \Phi^{(e)}}{4F C_{O2,\delta}\frac{D_{O2}}{\kappa}} = Da, \frac{\Delta C_e}{C_{e,0}} = 4(1 - t_+^0)\frac{C_{O2,\delta} D_{O2}}{C_{e,0}D_{Ce}}Da,$$

$$\text{and } \Delta T = 4F(E' - V_{cell})\frac{D_{O2}^{eff}}{k^{eff}}C_{O2,\delta} Da \tag{7}$$

Da is approximately 0.04 for 0.1 mA/cm^2 or 1 A/m^2, δ of 0.1 mm, ε of 0.75, τ_d of 1.5, D_{O2} of 10^{-9} m^2/s and $C_{O2,\delta}$ of 5 mol/m^3 (5 mM). This D_a will yield an oxygen concentration variation of ~4%. For other quantities such as T and $\Phi^{(e)}$, their variations are also small under Da of ~0.04 and common conditions, such as k^{eff} of ~1 W/m K and κ of ~0.001 S/cm.

In air cathodes, the actual electrochemical reaction kinetics and paths of the oxygen reduction reaction (ORR) are complex, involving a number of reaction steps and intermediates. For the ORR in dimethyl sulfoxide (DMSO)/LiPF$_6$ Electrolytes, the following steps were suggested [28]:

$$\begin{aligned} &\text{step1}: O_2 + Li^+ e^- = LiO_2 \\ &\text{step2}: 2LiO_2 = Li_2O_2 + O_2 = (\text{chemical}) \\ &\text{step3}: LiO_2 + Li^+ + e^- = Li_2O \\ &\text{step4}: Li_2O_2 + 2Li^+ + 2e^- = 2Li_2O \end{aligned}$$

$$(8)$$

For the sake of simplification, a one-step reaction is assumed with the discharge reaction rate approximated by the Tafel equation:

$$j_c = -ai_c = -ai_{0,c}^{ref}C_{O_2}^{1-\beta}C_e^{1-\beta}\exp\left(-\frac{1-\beta}{RT}F\eta\right) \tag{9}$$

where a represents the surface-to-volume ratio, determined by the electrode roughness. The surface overpotential η is determined by the local phase potentials and equilibrium potential U_o:

$$\eta = \Phi^{(s)} - \Phi^{(e)} - U_o \tag{10}$$

The above considers no precipitates deposited at the reaction surface. For a sufficiently small Da, the spatial variations of temperature, phase potentials, oxygen concentration, and C_e are negligibly small, thus the exchange current density j_c can be treated uniform across the entire thickness of the air cathode.

3. Oxygen Transport

In air cathodes, liquid electrolyte occupies the pore network. Oxygen is dissolved in the electrolyte at the electrolyte-gas interface, and then transported to the reaction surface for consumption during discharge. The 1-D transport equation is written as follow [27]:

$$\frac{\partial \varepsilon C_{O2}}{\partial t} + \frac{\partial u C_{O2}}{\partial x} = \frac{\partial}{\partial x}\left(D_{O2}^{eff}\frac{\partial C_{O2}}{\partial x}\right) + \frac{j_c}{4F} \tag{11}$$

In common operation, the mass consumption by the electrochemical reactions is negligibly small for promoting any considerable mass flow. Thus, the convection term can be neglected. Time constant analysis [26] indicated that the transient term can be

Table 2
Oxygen diffusivity in nonaqueous electrolytes [22].

Oxygen diffusivity	Electrolyte	Reference
7.0×10^{-6} cm^2/s	1 M LiPF$_6$ in PC:DME (1:1)	[47]
$4.0 - 4.5 \times 10^{-5}$ cm^2/s	CCl$_4$	[48]
$5.1 - 5.5 \times 10^{-5}$ cm^2/s	CS$_2$	[49]
$2.9 - 3.4 \times 10^{-5}$ cm^2/s	C$_2$H$_4$CL$_2$	[48]
$1.3 - 1.7 \times 10^{-5}$ cm^2/s	CH$_2$CL$_2$	[48]
9.75×10^{-6} cm^2/s	0.1 M TBAPF$_6$ in DMSO	[28]
2.45×10^{-5} cm^2/s	0.1 M TBAPF$_6$ in MeCN	[28]
1.67×10^{-5} cm^2/s	0.1 M LiPF$_6$ in DMSO	[28]
4.64×10^{-6} cm^2/s	0.1 M LiPF$_6$ in MeCN	[28]
1.22×10^{-5} cm^2/s	0.1 M LiPF$_6$ in DME	[28]
3.88×10^{-6} cm^2/s	0.1 M TBAPF$_6$ in DME	[28]
2.17×10^{-6} cm^2/s	0.1 M LiPF$_6$ in TEGDME	[28]
4×10^{-5} cm^2/s	1 M Li$^+$ in DME	[9]
9×10^{-6} cm^2/s	1 M Li$^+$ in PC:DME(1:2)	[9]
2.2×10^{-6} cm^2/s	1 M L:i$^+$ in PC	[9]
2.2×10^{-5} cm^2/s	0.1 M TBAClO$_4$	[4]
2.1×10^{-5} cm^2/s	0.1 M TBAPF$_6$	[4]
4.87×10^{-5} cm^2/s	0.9 M TEABF$_4$	[49]
2.07×10^{-5} cm^2/s	0.1 M TEAP	[50]

neglected, comparing with the single discharge timescale. One will then reach the below equation:

$$\frac{d}{dy}\left(D_{O2}^{eff}\frac{dC_{O2}}{dy}\right) = k\,C_{O2}^{\,1-\beta}$$

$$\text{where } k = \frac{ai_{0,c}^{ref}C_e^{1-\beta}}{4F}\exp\left(-\frac{1-\beta}{RT}F\eta\right) \quad (12)$$

The boundary conditions are written as:

$$\frac{dC_{O2}(0)}{dy} = 0 \text{ and } C_{O2}(\delta) = C_{O2,\delta} \quad (13)$$

Oxygen diffusivity in liquid electrolytes can be evaluated using a hydrodynamic model, which assumes that the resistance of solute molecule movement arises from the viscous force, similar to the particle movement in viscous fluids. In a dilute liquid, the hydrodynamic approach results in the famous Stokes–Einstein equation:

$$D_{O2} = \frac{k_B T}{6\pi r \mu} \quad (14)$$

where k_B is the Boltzmann's constant, r the oxygen molecular radius, and μ the electrolyte viscosity. Using the Stokes-Einstein equation, the oxygen diffusivity ranges from 10^{-11} to 10^{-8} m^2/s. Table 2 summarizes oxygen diffusivity in a few electrolytes.

For general cases, the above problem of oxygen transport is written in the dimensionless form as:

$$\frac{d}{d\overline{y}}\left(\frac{d\overline{C}_{O2}}{d\overline{y}}\right) = 2Da\cdot\overline{C}_{O2}^{\,1-\beta} \quad (15)$$

where a more general Damköhler (D_a) number is defined as

$$Da = \frac{k\delta^2}{2D_{O2}^{eff}C_{O2,0}^{\,\beta}} = \frac{\text{Reaction rate}}{\text{Mass transport rate}}$$

Boundary conditions: $\frac{d\overline{C}_{O2}(0)}{d\overline{y}} = 0$ and $\overline{C}_{O2}(1) = 1$

For β=0 and 1, one can solve directly the problem:

For $\beta = 1$

$$: \overline{C}_{O2} = 1 - Da(1-\overline{y}^2)\text{For }\beta = 0 : \overline{C}_{O2} = \frac{\cosh(\sqrt{2Da}\,\overline{y})}{\cosh(\sqrt{2Da})} \quad (16)$$
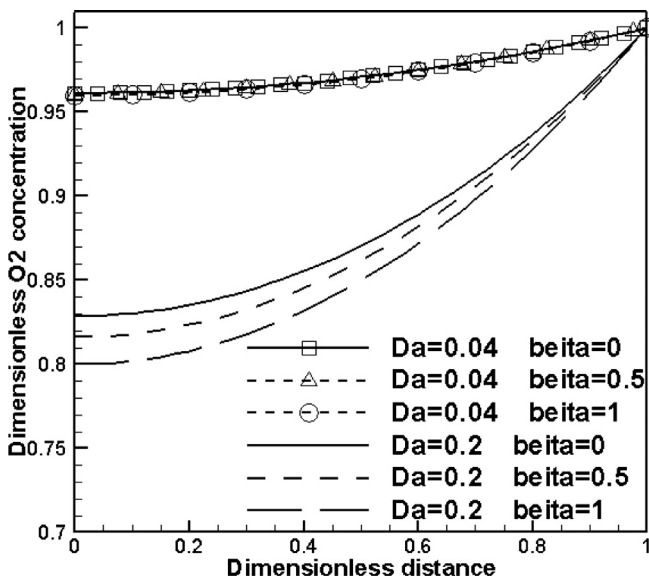

Fig. 2. Oxygen profiles in an air cathode under different Da and β.

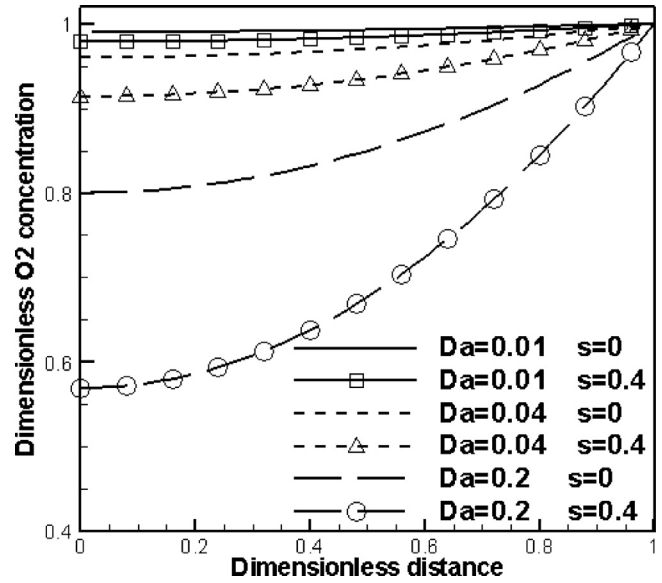**Fig. 3.** Oxygen profile in an air cathode under β=0.5 and two levels of the Li oxide volume fraction.

For the case of β=0.5, which was adopted by a few studies [19,23], the problem is nonlinear and can be solved through numerical iterative methods. In addition, using perturbation analysis, one can define a small parameter ε=Da, and write the solution in the form of a formal power series or perturbation series (as $\overline{C}_{O2} = \sum_{n=0}^{\infty} a_n \varepsilon^n$), and solve a_0 and a_1 for an approximate solution with an accuracy of $O(\varepsilon^2)$ or $O(Da^2)$. The perturbation solution is found to be the same as the exact solution to β=1, as shown in Eq. (16).

Fig. 2 plots the oxygen profiles in an air cathode, showing that under the Da of 0.04, oxygen variation is small <5%; and the oxygen profiles are almost identical for the three selections of β value. There is appreciable discrepancy among the three under the Da number of 0.2, but less than 3%.

Local oxygen consumption and discharge product generation are determined by the local electrochemical reaction, which in turn depends on local oxygen content and discharge product volume fraction. Li oxides precipitate in the pore network and narrow down the passage, reducing the effective oxygen diffusivity. Assuming the film is firmly packed without any pore structure, the effective diffusivity can be modified following the Bruggeman correlation:

$$D_{O2}^{eff} = \varepsilon^{\tau_d}D_{O2}^0 = (\varepsilon_0 - \varepsilon_{prod})^{\tau_d}D_{O2}^0 = \varepsilon_0^{\tau_d}(1-s)^{\tau_d}D_{O2}^0 \quad (17)$$

where τ_d represents the diffusion path's tortuosity, ε_0 the initial porosity of an air cathode in absence of oxide precipitate, and ε_{prod} the volume fraction of oxide precipitate inside pores.

Analytically solving this electrochemically coupled transport problem is challenging, particularly when the effects of oxide precipitate on oxygen diffusivity and consumption are taken into account. One method is to evaluate the associated voltage loss by assuming the cathode consists of a number of independent reactors operated under constant current, as done in in PEM fuel cells [27,29]. As the reaction is uniform, the local reaction rate $j_c = -\frac{I}{\delta}$; and the oxygen concentration is analytically obtained as below:

$$\overline{C}_{O2}(\overline{y}) = 1 - Da\frac{1-\overline{y}^2}{\varepsilon_0^{\tau_d-\tau_{d,0}}\left(1-\frac{\varepsilon_{prod}}{\varepsilon_0}\right)^{\tau_d}} = 1 - Da\frac{1-\overline{y}^2}{\varepsilon_0^{\tau_d-\tau_{d,0}}(1-s)^{\tau_d}} \quad (18)$$
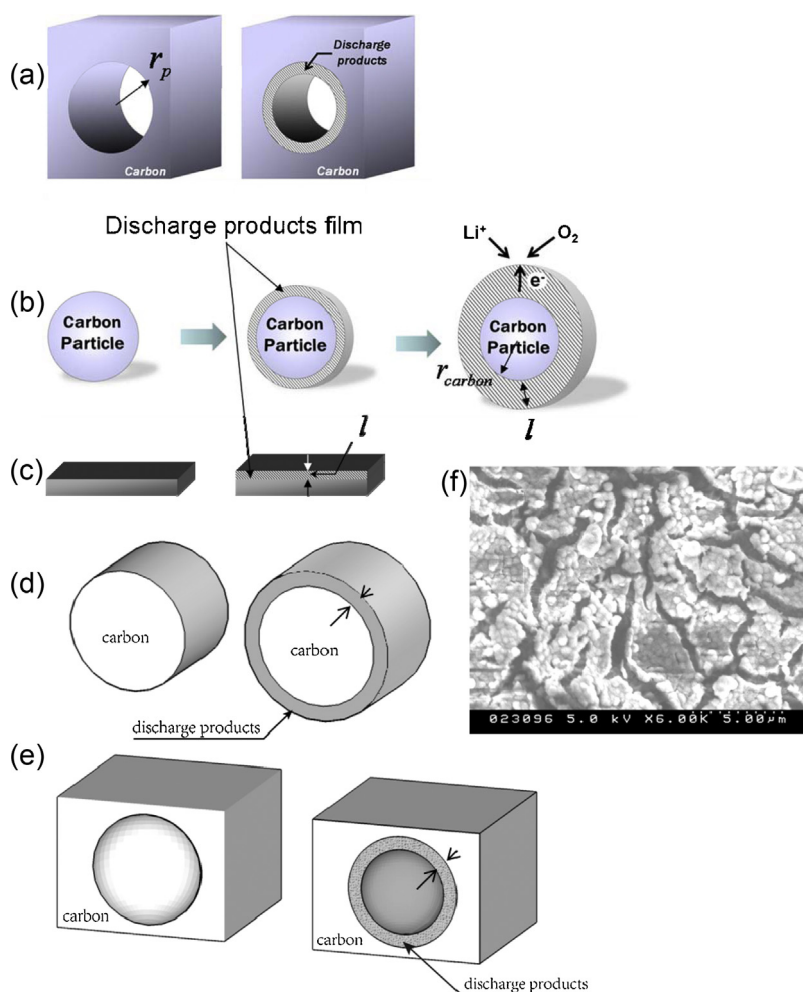
Fig. 4. Typical growth modes of the oxide precipitate film in air cathodes: a.) the inward cylindrical-film growth mode; b.) the outward spherical-film growth mode; c.) the planar-film growth mode; d.) the outward cylindrical-film mode; e.) the inward spherical-film mode; f.) the SEM image of precipitate on highly ordered pyrolytic graphite (HOPG) at 10 μA/cm^2 for 1 M LiTriflate in DOL:DME (1:1 w/w) [22].

Fig. 3 plots the oxygen profiles under various Da and oxide precipitate's volume fractions. The oxygen spatial variation is larger when oxide precipitate is present, as a result of the increased oxygen transport resistance. For Da of 0.2 and s of 0.4, the local oxygen content varies by >40%. For Da of 0.04 and s of 0.4, the variation is still small within 10%. For Da of 0.01, the precipitate's effect is about 1%.

Table 3
Physical, electrochemical, and model parameters.

Description	Unit	Value
Temperature	°C	25
Transfer coefficient β		0.5
Faraday constant	C/mol	96,487
Electrical conductivity of cathode electrode	S/m	~10
O$_2$ diffusivity in electrolyte	m^2/s	9×10^{-10}
Equilibrium oxygen concentration (case 1/case 2)	mol/ m^3	2.30/4.33
Cathode thermal conductivity	W/m K	~1.0
Tortuosity τ		1.8
Electrode porosity, ε_0		0.75
Electrode thickness, δ	mm	0.5/0.75
Density of discharge product (Li$_2$O$_2$/ Li$_2$CO$_3$)	kg/ m^3	2227/2310
Molecular weight of discharge product (Li$_2$O$_2$/Li$_2$CO$_3$)	kg/mol	0.04044/0.04588
A_0	Ω m^2	8.5×10^7
I_0	A m^{-2}	0.5
B_1 in Eq. (22) [23]		2.5
B_2 in Eq. (22) (case 1 and case 3 [23]/case 2 [26])		8/12
s_0 in Eq. (22) [26]		0.2

4. Surface Coverage Mode

During discharging, insoluble Li oxides are produced and deposited at local reaction sites. It is likely the initial precipitate nucleates heterogeneously at preferred sites, followed by thin film formation over the surface. Film formation was experimentally observed over flat electrodes, see Fig. 4 (f). The deposit film has low electric conductivity, resisting electrons to react with Li$^+$ and oxygen. Fig. 4 sketches a few typical modes of film growth. A porous electrode consists of reaction surfaces of various morphologies. Thus, the film growth is complex. The below power law is frequently adopted to describe the reaction surface reduction arising from precipitate [29]:

$$a = a_0(1 - \frac{\varepsilon_{prod}}{\varepsilon_0})^{\tau_a} \qquad (19)$$

where τ_a is the surface coverage coefficient; and the volume of precipitate ε_{prod} is calculated through the reaction rate:

$$\varepsilon_{prod} = \int_0^t -\frac{j_c M_{prod}}{nF\rho_{prod}}dt = \varepsilon_{prod,0} + \frac{IM_{prod}}{n\delta F\rho_{prod}}t \qquad (20)$$

in which n denotes the moles of electrons transferred per mole of the oxide. Note that the above equation also describes discharge deposit consisting of different Li compounds by using an average n and average density ρ_{prod}. Our model validation, to be presented in the next section, accounts for both Li_2O_2 and Li_2CO_3 as discharge products. Similar approach was also adopted in Ref. [19].

The above coverage model is more general, encompassing the film resistor model. Wang [23] provides detailed derivation of the surface coverage factor from the film resistance. For the spherical-film growth mode, the exponent coefficient τ_a is given by [23]:

$$\tau_a = -\frac{I(1-\beta)F}{a_0 RT \ln\left(1 - \frac{\varepsilon_{prod}}{\varepsilon_0}\right)}\left\{A_0\left[1/3\sqrt{1 + \frac{\varepsilon_{prod}}{\varepsilon_{carbon}}} - 1\right]r_{carbon} + R_0\right\} \qquad (21)$$

The above equation indicates that τ_a is a function of the current density I and ε_{prod}. For porous electrodes which contain various morphologies of reaction sites, the following correlation was proposed by Wang [23]:

$$\tau_a = \begin{cases} B_1\frac{I}{I_0} & s < s_0 \text{ where } s = \frac{\varepsilon_{prod}}{\varepsilon_0} \\ \frac{I}{I_0}[B_1 + B_2(s - s_0)] & \text{otherwise} \end{cases} \qquad (22)$$

The above formula is developed through two approximates, the first is as s→0; the other is the slope as s→s$_0$. For the spherical-film growth mode and R_0=0, the parameters are given by:

$$B_1 = \frac{(1-\beta)FA_0 r_{carbon}\varepsilon_0 I_0}{3a_0 RT\varepsilon_{carbon}} \text{ and}$$

$$B_2\frac{(1-\beta)FA_0 r_{carbon}I_0}{a_0 RT}\left(\frac{\varepsilon_0/\varepsilon_{carbon}}{3\ln(1-s_0)(\frac{s_0\varepsilon_0}{\varepsilon_{carbon}}+1)^{2/3}} + \frac{(s_0\varepsilon_0/\varepsilon_{carbon}+1)^{1/3}-1}{(1-s_0)(\ln(1-s_0))^2}\right) \qquad (23)$$

5. Discharge Voltage Loss

The oxygen profile of Eq. (18) is substituted into Eq. (9), yielding the below overpotential change [27]:

$$\Delta\eta = \frac{RT}{(1-\beta)F}\left(\tau_a \ln(1-s) + (1-\beta)\ln\left(1 - Da1 - \frac{\bar{y}^2}{\varepsilon_0^{\tau_d-\tau_{d,0}}(1-s)^{\tau_d}}\right)\right)$$

$$= \Delta\eta_a + \Delta\eta_{O2}$$

where

$$\Delta\eta_a = \frac{RT\tau_a\ln(1-s)}{(1-\beta)F} \text{ and } \Delta\eta_{O2} = \frac{RT}{F}\ln\left(1 - Da1 - \frac{\bar{y}^2}{\varepsilon_0^{\tau_d-\tau_{d,0}}(1-s)^{\tau_d}}\right) \qquad (24)$$

The voltage loss due to the oxygen transport resistance raised by oxide precipitate can be assessed through the overpotential at the middle thickness, i.e.

$$\Delta\eta_{O2}(\bar{y} = 0.5) = \frac{RT}{F}\ln\left(1 - \frac{3Da}{4\varepsilon_0^{\tau_d-\tau_{d,0}}(1-s)^{\tau_d}}\right) \qquad (25)$$

For a crude evaluation, the total voltage loss associated with oxide precipitate, i.e. the raised oxygen transport polarization and
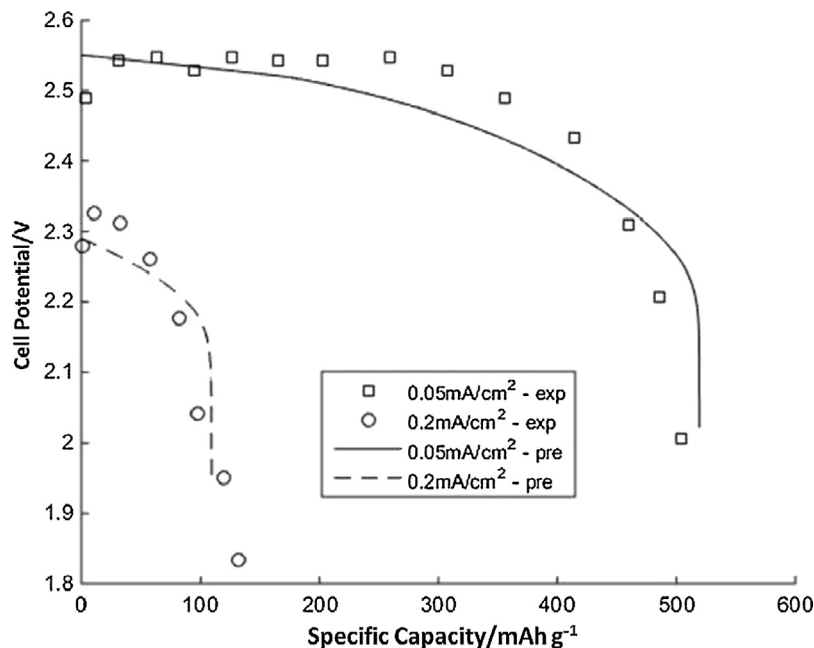

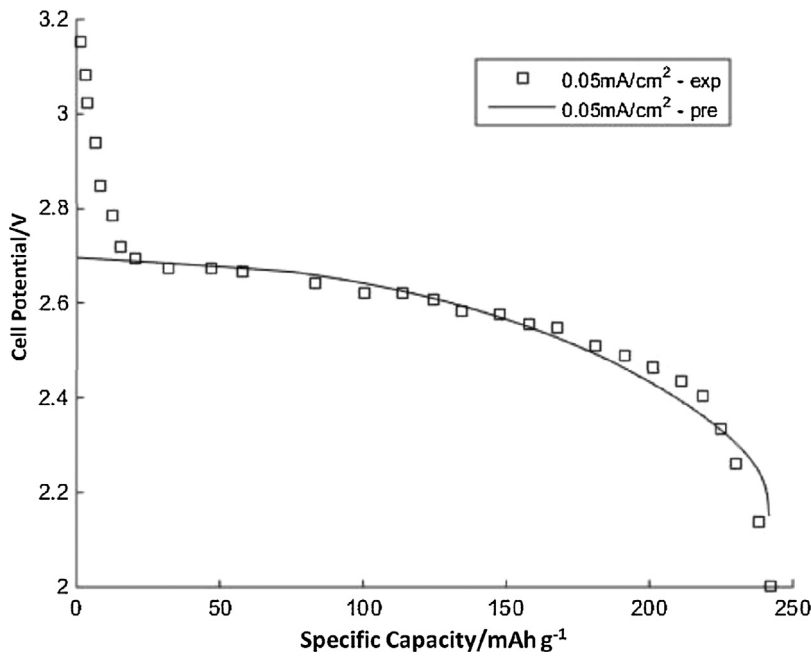**Fig. 5.** Comparison of the model prediction with experimental data (case 1) [30].

Fig. 6. Comparison of the model prediction with experimental data (case 2) [31].

electric passivation, can be approximated by:

$$\Delta\eta = \Delta\eta_a + \Delta\eta_{O2}(\overline{y} = 0.5) \tag{26}$$

In the below comparison with experimental data, a similar set of model parameters were used for all the cases, listed in Table 3. Figs. 5–7 present comparison with experimental data from Zhang and Read [30] (case 1), Sahapatsombut et al. [31] (case 2), and Shui et al. [32] (case 3), respetively, showing acceptable agreements: the first stage of gradual decrease arises primarily from electrode passivation due to oxide precipitation at the reaction surface; the latter precipitous drop is mainly caused by the oxygen transport resistance due to Li oxides occupying the cathode's pore space. In Fig. 6, the initial rapid drop observed in the experiment was likely due to other mechanisms, not raised by oxide precipitation.A few parameters, including Da, tortuosity τ_d, and surface coverage factor τ_a, greatly impact the voltage evolution and capacity loss. As discharge proceeds, the volume fraction of oxide precipitate, s, increases until reaching the cut-off voltage V_{cut}. Thus, s_{max} occurs
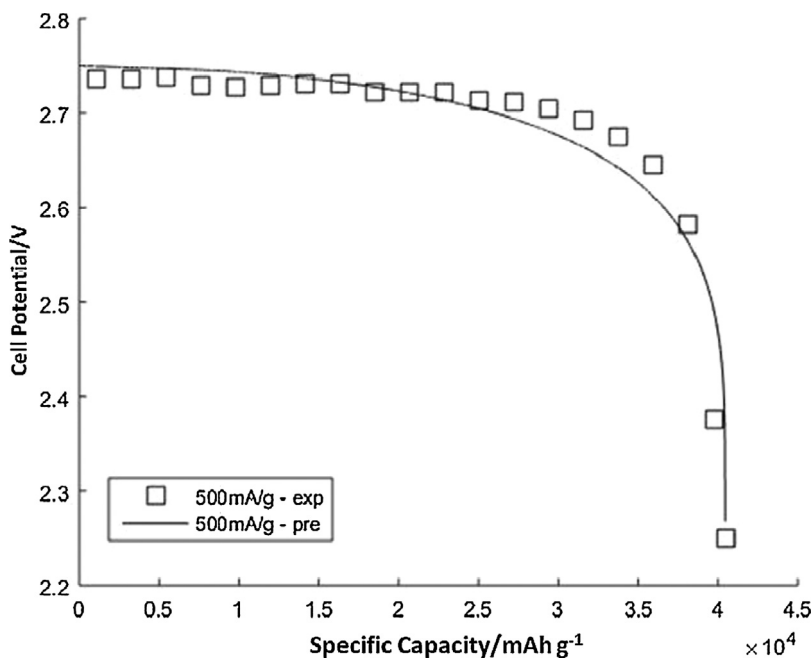

Fig. 7. Comparison of the model prediction with experimental data (case 3) [32].
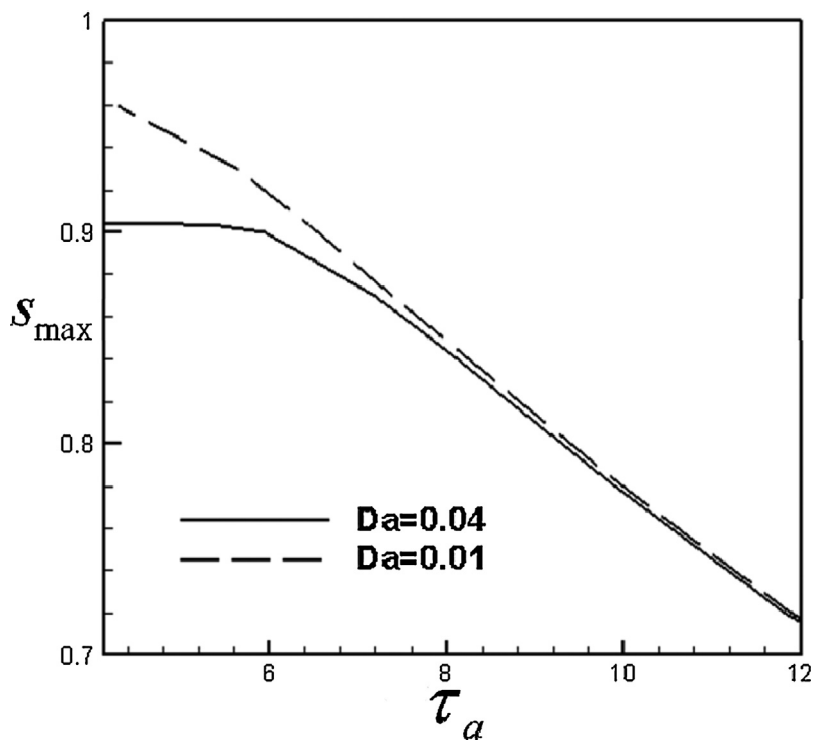
Fig. 8. s_{max} as a function of τ_a under β of 0.5, τ_d of 1.5, V_o of 2.75 V and V_{cut} of 2.0. V. s_{max} and τ_a represent the storage capacity and coverage coefficient of Li oxide deposit in air cathode, respectively.
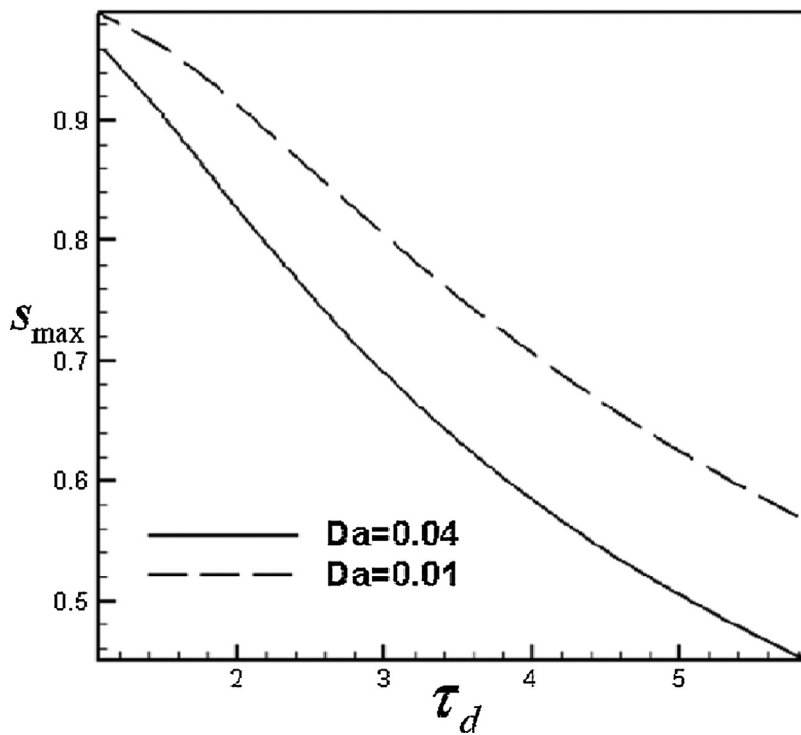

Fig. 9. s_{max} as a function of τ_d under β of 0.5, τ_a of 2.5, V_o of 2.75 V and V_{cut} of 2.0 V. s_{max} and τ_d represent the storage capacity Li oxide deposit and tortuosity of air cathode, respectively.

Table 4
MacMullin number (N_M) of a system consisting of a dispersed non-conducting phase in a conductive medium [29,51].

Label	Geometry	Arrangement	Size	Expression
I	Spheres	Random	Uniform	$N_M = \frac{(5-\varepsilon)(3+\varepsilon)}{8(1+\varepsilon)\varepsilon}$
II	Spheres	Cubic lattice	Uniform	$N_M = \frac{(3-\varepsilon)\left[\frac{4}{3}+0.409(1-\varepsilon)^{7/3}\right]-1.315(1-\varepsilon)^{10/3}}{2\varepsilon\left[\frac{4}{3}+0.409(1-\varepsilon)^{7/3}\right]-1.315(1-\varepsilon)^{10/3}}$
III	Spheres	Random and ordered	Range	$N_M = \varepsilon^{-1.5}$
IV	Cylinders	Parallel (square array)	Uniform	$N_M = \frac{2-\varepsilon-0.3058(1-\varepsilon)^4-1.334(1-\varepsilon)^8}{\varepsilon-0.3058(1-\varepsilon)^4-1.334(1-\varepsilon)^8}$
V	Fibrous material (Cylinders)	Random	–	$N_M = \frac{0.9126}{\varepsilon(\varepsilon-0.11)^{0.785}}$

at the cut-off voltage, and is closely linked to the battery's energy density providing that the extra space 1-s_{max} cannot be used for storing the oxide. By reducing 1-s_{max} or increasing s_{max}, the battery's energy density will be improved.

From Eq. (26), one can develop a formula for s_{max} by assuming the voltage loss is caused by oxide precipitate:

$$\frac{RT}{(1-\beta)F}\left(\tau_a\ln(1-s_{max})+(1-\beta)\ln\left(1-Da\frac{3}{4[(1-s_{max})]^{\tau_d}}\right)\right)$$
$$= -(V_o - V_{cut}) \tag{27}$$

where V_o and V_{cut} denote the voltages at s=0 and s=s_{max}, respectively. By rearrangement, one will reach:

$$(1-s_{max})^{\tau_a}\left(1-Da\frac{3}{4(1-s_{max})^{\tau_d}}\right)^{1-\beta}$$
$$= \exp\left(-\frac{(1-\beta)F(V_o-V_{cut})}{RT}\right) \tag{28}$$

For any given operation, i.e. V_o and V_{cut} are constant, the above formula directly shows s_{max} as a function of a few key parameters. Though solving s_{max} is implicit, the formulas can be rearranged to

inversely relate s_{max} to those parameters as below:

$$\tau_a = \frac{\left(-\frac{(1-\beta)F(V_o-V_{cut})}{RT}\right)-(1-\beta)\ln\left(1-Da\frac{3}{4[(1-s_{max})^{\tau_d}]}\right)}{\ln(1-s_{max})}\tau_d$$

$$= \frac{\ln\left\{\dfrac{3}{4}\dfrac{Da}{1-\left[\dfrac{\exp\left(\frac{(1-\beta)F(V_o-V_{cut})}{RT}\right)}{(1-s_{max})^{\tau_a}}\right]^{1/(1-\beta)}}\right\}}{\ln(1-s_{max})}Da$$

$$= \frac{4}{3}[(1-s_{max})]^{\tau_d}\left\{1-\left[\frac{\exp\left(-\frac{(1-\beta)F(V_o-V_{cut})}{RT}\right)}{(1-s_{max})^{\tau_a}}\right]^{1/(1-\beta)}\right\} \tag{29}$$

Fig. 8 plots the relationship between s_{max} and τ_a under two Da numbers, β of 0.5, τ_d of 1.5, V_o of 2.75 V and V_{cut} of 2.0 V. In PEM fuel cells, the parameter τ_a measures the degree of the produced ice precipitate's impact on the active reaction surface. Local ice morphology at the reaction site likely changes as ice volume increase: from the initial heterogeneous growth to latter film growth. As a result, τ_a may vary with the volume fraction of precipitate [24]. In Li-air battery, the parameter τ_a is defined to account for the resistance of oxide precipitate to electron transport, i.e. passivation. It varies with the current density, the
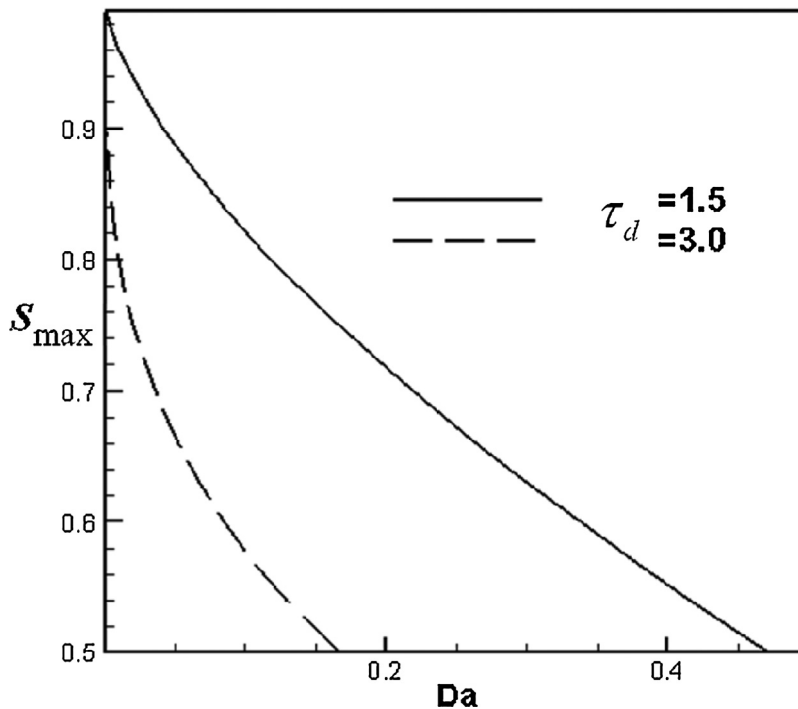

Fig. 10. s_{max} as a function of Da under β of 0.5, τ_d of 1.5, τ_a of 2.5, V_o of 2.75 V and V_{cut} of 2.0 V. s_{max} and Da represent the storage capacity of Li oxide deposit and the Damköhler Number, respectively.

volume fraction of oxide precipitate, oxide's electric resistance, and a few other factors such as the reaction surface's area and morphology. In addition, it is likely that the Li oxide deposit appears in form of initial isolated islands, followed by thin film over reaction surface, similar to ice formation in PEM fuel cells. Eq. (22) accounts for the two situations by defining different τ_a functions and the transition s_0. Note that the isolated island shape describes several morphologies, e.g. adjusting the island size and volume-to-surface ratio. In this figure, we consider τ_a as an independent variable, representing the value of τ_a at s_{max}. It is seen that s_{max} is reduced as τ_a increases. The difference between the two Das is small when τ_a is over 7. As τ_a becomes smaller than 6, the difference is evident, with the Da of 0.04 reaching a limit of s_{max} around 0.9 and the Da of 0.01 exhibiting a continuing increase as τ_a further decreases.

Fig. 9 plots the relationship between s_{max} and τ_d under the two Da numbers, β of 0.5, τ_a of 2.5, V_o of 2.75 V and V_{cut} of 2.0 V. In porous media, tortuosity τ_d measures the actual length of diffusion passage in a porous medium. In addition, the MacMullin number (N_M), defined as the ratio of resistance of porous media saturated with an electrolyte to the bulk resistance of the same electrolyte:

$$N_M = \frac{D_k}{D_k^{eff}} = \frac{1}{f(\varepsilon, \tau_d)} \tag{30}$$

In Eq. (4), the MacMullin number is implicitly defined as $\varepsilon^{-\tau}$. Table 4 lists the expression of N_M for various porous media as a function of ε. In general, $f(\varepsilon, \tau_d)$ is determined by the pore structure such as its morphology and arrangement. In some structures, e.g. the fiber matrix in carbon papers, the tortuosity of electron passage can be over 10. Fig. 9 shows that as τ_d increases, the effective transport resistance enlarges, thus s_{max} is reduced. The difference between the two Das is evident as shown by the two curves. s_{max} reaches over 90% as τ_d is below 2.0. A large τ_d, though benefiting the reaction surface area due to the highly torturous structure, yields a big resistance to oxygen transport as the oxide precipitate accumulates.

Fig. 10 plots the relationship between s_{max} and Da under β of 0.5, τ_a of 2.5, V_o of 2.75 V, and V_{cut} of 2.0 V. As defined by Eq. (15), Da represents the ratio of the reaction rate to oxygen transport rate, characterizing the operation of a chemical reactor. To fully utilize the pore space in cathode, Da should be kept low in order to avoid considerable spatial variations in the reaction rate and hence in the oxide precipitate's content. This figure shows as Da increases (i.e. the transport resistance relative to the reaction rate enlarges), s_{max} is reduced, as expected. The difference between the two τ_ds is evident as shown by the two curves. s_{max} is rapidly reduced to below 50% as Da approaches 0.2 under τ_d of 3.0. Solid oxide precipitate accumulates inside the pore network, narrowing down the diffusive passage. A larger τ_d will yield a bigger influence of oxide precipitate, and consequently a smaller oxide storage capacity of air cathode.

6. Conclusions

In this work, we analytically obtained oxygen profiles, formulated the variations of several quantities as a function of Da, evaluated discharge voltage loss, and formulated the Li oxide's storage capacity in the air cathode of Li-air batteries. The spatial variations of important quantities including temperature, species concentrations, and phase potentials were formulated using a single dimensionless parameter, Da. Specially, the oxygen concentration variation is found equal to Da; and the formulas quantitatively measure how low Da should be in order to achieve nearly uniform distributions of these quantities. The oxygen profiles were analytically obtained under various conditions, and we found that the oxygen profiles for the three reaction orders are similar under low Da. A model was proposed to evaluate the voltage loss due to the oxygen transport resistance arising from oxide accumulation, indicating that the precipitate can greatly influence the oxygen profile under a large Da, e.g. Da>0.04. An approximation model was formulated to evaluate the discharge voltage loss due to oxide precipitation, showing acceptable agreement with experimental data. Furthermore, analytical formula were developed to explicitly express the Li oxide storage capacity s_{max}, which is closely related to the battery energy density, as a function of several parameters including surface coverage factor, tortuosity, and Da. The derived analytical formula can be applied for cathode optimization through cathode structural properties, such as thickness, the pore structure (porosity and tortuosity), surface area, and electrolyte composition, and operation condition such as current density and oxygen concentration.

References

[1] P.G. Bruce, S.A. Frauberger, L.J. Hardwick, J.-M. Tarascon, Nat. Mater. 11 (2012) 19.
[2] K.M. Abraham, Z. Jiang, J. Electrochem. Soc. 143 (1996) 1.
[3] Y. Gao, C. Wang, W. Pu, Z. Liu, C. Deng, P. Zhang, Z. Mao, Int. J. of Hydrogen Energy 37 (17) (2012) 12725.
[4] C.O. Laoire, S. Mukerjee, K.M. Abraham, J. Phys. Chem. C 113 (2009) 20127.
[5] Y. Li, J. Wang, X. Li, D. Geng, R. Li, X. Sun, Chem. Comm. 47 (2011) 9438.
[6] A. Debart, J. Bao, G. Armstrong, P.G. Bruce, J. Power Sources 174,1177 (2007) .
[7] Y. Lu, Z. Xu, H.A. Gasteiger, S. Chen, K. Hamad-Schifferli, Y. Shao-Horn, J. Am. Chem. Soc. 132 (2010) 12170.
[8] Y. Lu, H.A. Gasteiger, M.C. Parent, V. Chiloyan, Y. Shao-Horn, Electrochem. Solid-State Lett. 13 (2010) A69.
[9] Y.C. Lu, D.G. Kwabi, K.P.C. Yao, J.R. Harding, J. Zhou, L. Zuin, Y. Shao-Horn, Energy & Environmental Science 4 (2011) 2999.
[10] M. Mirzaeian, P.J. Hall, Electrochim. Acta 54 (7444) (2009) .
[11] X. Yang, P. He, Y. Xia, Electrochem. Comm 11 (6) (2009) 1127.
[12] R.R. Mitchell, B.M. Gallant, C.V. Thompson, S.H. Yang, Energy Environ. Sci. 4 (2011) 2952.
[13] L.D. Griffith, A. Sleightholme, J.F. Mansfield, D.J. Siegel, C.W. Monroe, ACS Appl. Mater. Interfaces (2015) , doi:http://dx.doi.org/10.1021/acsami.5b00574 Accepted Manuscript.
[14] J. Xiao, D. Wang, W. Xu, R.E. Williford, J. Liu, J. Zhang, J. Electrochem. Soc. 157 (4) (2010) A487–A492.
[15] S.S. Zhang, D. Foster, J. Read, J. Power Sources 195 (2010) 1235.
[16] V. Viswanathan, K.S. Thygesen, J.S. Hummelshøj, J.K. Nørskov, G. Girishkumar, B.D. McCloskey, A.C. Luntz, J. Chem. Phys. 135 (2011) 214704.
[17] A.A. Franc, K.-H. Xue, Carbon-based electrodes for lithium air batteries: scientific and technological challenges from a modeling perspective, ECS Journal of Solid State Science and Technology 2.10 (2013) M3084–M3100.
[18] P. Andrei, J.P. Zheng, M. Hendrickson, E.J. Pichta, J. Electrochem. Soc 157 (12) (2010) A1287.
[19] P. Albertus, G. Girishkumar, B. McCloskey, R.S. Sanchez-Carrera, B. Kozinsky, J. Christensen, A.C. Luntz, J. Electrochem. Soc. 158 (2011) A343.
[20] S. Sandhu, J. Fellner, G. Brutchen, J. Power Sources 164 (2007) 365.
[21] J. Nanda, H. Bilheux, S. Voisin, G.M. Veith, R. Archibald, L. Walker, S. Allu, N.J. Dudney, S. Pannala, J, Phys. Chem. C 116 (15) (2012) 8401–8408.
[22] Y. Wang, S.C. Cho, Analysis and Multi-Dimensional Modeling of Lithium-Air Batteries, Journal of The Electrochemical Society 162 (1) (2015) A114–A124.
[23] Y. Wang, Electrochimica Acta 75 (2012) 239.
[24] J. Mishler, Y. Wang, P.P. Mukherjee, R. Mukundan, R.L. Borup, Electrochimica Acta 65 (2012) 127.
[25] Y. Wang, P.P. Mukherjee, J. Mishler, R. Mukundan, R.L. Borup, Electrochimica Acta 55 (2010) 2636.
[26] Y. Wang, S.C. Cho, Analysis of Air Cathode Performance for Lithium-Air Batteries, Journal of The Electrochemical Society 160 (10) (2013) A1847–A1855.
[27] Y. Wang, J. Electrochem. Soc. 154 (2007) B1041.
[28] C. O'Laoire, S. Mukerjee, K.M. Abraham, E.J. Plichta, M.A. Hendrickson, J. Phys. Chem. C, J. Phys. Chem. C 114 (2010) 9178.
[29] Y. Wang, K.S. Chen, S.C. Cho, PEM Fuel Cells: Thermal and Water Management Fundamentals, Momentum Press, 2013.

[30] S.S. Zhang, J. Read, Partially fluorinated solvent as a co-solvent for the non-aqueous electrolyte of Li/air battery, Journal of Power Sources 196 (5) (2011) 2867–2870.
[31] U. Sahapatsombut, H. Cheng, K. Scott, Modelling of operation of a lithium-air battery with ambient air and oxygen-selective membrane, Journal of Power Sources 249 (2014) 418–430.
[32] J. Shui, F. Du, C. Xue, Q. Li, L. Dai, Vertically Aligned N-Doped Coral-like Carbon Fiber Arrays as Efficient Air Electrodes for High-Performance Nonaqueous Li–O2 Batteries, ACS nano 8 (3) (2014) 3015–3022.
[33] H.A. Every, F. Zhou, M. Forsyth, D.R. MacFarlane, Electrochimica Acta 43 (1998) 1465.
[34] N. Nithya, S. Selvasekarapandian, P.C. Selvin, D.A. Kumar, J. Kawamura, Electrochimica Acta 66 (1) (2012) 110.
[35] S. Rajendran, M. Sivakumar, R. Subadevi, Materials Letters 58 (2004) 641.
[36] K.M. Abraham, S.B. Brummer, in: J.P. Gabano (Ed.), Lithium Batteries, Academic Press, New York, 1983, pp. 371.
[37] H.J. Rhoo, H.T. Kim, J.K. Park, T.S. Hwang, Electrochimica Acta 42 (10) (1997) 1571.
[38] S. Rajendran, T. Mahalingam, R. Kannan, Solid State Ionics 130 (2000) 143.
[39] K.M. Abraham, M. Alamgir, J. Electrochem. Soc 137 (5) (1990) 1657.
[40] M. Watanabe, M. Kanba, K. Nagaoka, I. Shinohara, Journal of Polymer Science: Polymer Physics Edition 2 (1983) 939.
[41] N. Munichandraiah, G. Sivasankar, L.G. Scanlon, R.A. Marsh, J. Appl. Polym. Sci 65 (11) (1998) 2191.
[42] W. Xu, C.A. Angell, Electrochimica Acta 48 (2003) 2029.
[43] W.V. Schalkwijk, B. Scrosati, Advances in Lithium-Ion Batteries, Springer, 2002.
[44] P. Birke, S. Doring, S. Scharner, W. Weppner, Ionics 2 (1996) 329.
[45] W. Xu, C.A. Angell, Electrochimica Acta 48 (2003) 2029.
[46] X. Sun, X.Q., Yang, H.S., Lee, J. McBreen, Proc. of the 194th Electrochemical Society Meeting, BNL-66142, CONF-981108, Boston (1998).
[47] J. Read, K. Mutolo, M. Ervin, W. Behl, J. Wolfenstine, A. Driedger, D. Foster, J. Electrochem. Soc. 150 (2003) A1351.
[48] X.Z. Wu, T. Morikawa, K. Uchiyama, T. Hobo, J. Phys. Chem. B 101 (1997) 1520.
[49] S.-Y. Kishioka, Electroanalysis 13 (2001) 1161–1164.
[50] M. Tsushima, K. Tokuda, T. Ohsaka, Anal. Chem. 66 (1994) 4551–4556.
[51] M.J. Martínez, S. Shimpalee, J.W. Van Zee, Measurement of MacMullin Numbers for PEMFC Gas-Diffusion Media, Journal of The Electrochemical Society 156 (1) (2009) B80–B85.